RSC Advances

PAPER

View Article Online
View Journal | View Issue

Open Access Article. Published on 08 November 2019. Downloaded on 4/27/2026 3:35:23 PM.
This article is licensed under a Creative Commons Attribution 3.0 Unported Licence.

Check for updates

Cite this: *RSC Adv.*, 2019, **9**, 36434

Rapid room-temperature synthesis of ultrasmall cubic Mg–Mn spinel cathode materials for rechargeable Mg-ion batteries†

Hiroaki Kobayashi, *[a] Kazuya Yamaguchi [b] and Itaru Honma [a]

Received 12th September 2019
Accepted 1st November 2019

DOI: 10.1039/c9ra08626a

rsc.li/rsc-advances

Reducing the particle size of cathode materials is effective to improve the rate capability of Mg-ion batteries. In this study, ultrasmall cubic Mg–Mn spinel oxide nanoparticles approximately 5 nm in size were successfully synthesized *via* an alcohol reduction process within 30 min at room temperature. Though the particles aggregated to form large secondary particles, the aggregation could be suppressed by covering the particles with graphene. The composite exhibited a specific capacity of 230 mA h g^{-1}, and could be cycled more than 100 times without any large capacity loss even at a moderate current density with the $Mg(ClO_4)_2/CH_3CN$ electrolyte.

Introduction

High energy and high density rechargeable batteries are indispensable for widespread portable electronic devices and the spreading of electric vehicles. Currently, Li-ion batteries have been widely utilized for these high-power applications,[1] but to meet increasing requirements to enhance their energy densities, it is necessary to develop novel energy storage systems, such as Li–air,[2,3] Li–S,[2,4] and multivalent-ion batteries.[5] Rechargeable Mg-ion batteries have gained much attention as promising alternatives to Li-ion batteries due to the high natural abundance, high volumetric energy density, and no dendrite formation of the Mg metal anode.[6–9] While Mg-ion batteries are nowadays progressing rapidly, their practical use is still hampered by problems related to both cathode materials and electrolytes. One of the crucial problems is the very low rate capability at the cathodes due to the slow diffusion of Mg^{2+} ions in solids.[10] Therefore, most reported Mg-ion batteries work at low current densities or at high temperature. This problem could be solved using water-based or water-added electrolytes, but they are incompatible with Mg metal anodes.[6]

Among various cathode candidates for Mg-ion batteries, spinel oxides have a high redox potential and a relatively low diffusivity.[11] Especially in the common electrochemical window of electrolytes (<3.5 V *vs.* Mg/Mg^{2+}), $MgMn_2O_4$ can exhibit a high theoretical capacity of 540 mA h g^{-1} using both Mn^{3+}/Mn^{4+} and Mn^{3+}/Mn^{2+} redox according to the following reactions:

$$MgMn_2O_4 \rightleftarrows Mn_2O_4\ (\lambda\text{-}MnO_2) + Mg^{2+} + 2e^- \quad (1)$$

$$MgMn_2O_4 + Mg^{2+} + 2e^- \rightleftarrows Mg_2Mn_2O_4\ (\text{rock-salt}) \quad (2)$$

In eqn (1), extraction/insertion of Mg in a tetrahedral site proceeds with holding the host spinel structure, while a transformation reaction between $MgMn_2O_4$ spinel and $Mg_2Mn_2O_4$ rock-salt proceeds *via* push-out process in eqn (2).[12] Recently, $MgMn_2O_4$ with particle sizes of 11–200 nm were synthesized by various processes such as sol–gel and co-precipitation methods, and their cathode performances were investigated.[12–23] Some reports demonstrated high specific capacities, but so far, there are no reports where high capacity could be obtained at high rates with an anhydrous electrolyte under ambient temperature. Since decreasing the particle size is one of the most effective ways to enhance the specific capacity and the rate capability for suppressing the slow Mg^{2+} diffusion in solids,[24] alternative synthetic methods that enable nanoparticles below 10 nm are required for achieving a breakthrough in such cathodes.

In addition, the $MgMn_2O_4$ has a tetragonal spinel structure due to the Jahn–Teller effect of Mn^{3+} ions,[25] while λ-MnO_2 and $Mg_2Mn_2O_4$ rock-salt are cubic phase. The above redox reactions should exhibit large polarizations because of the less reversible tetragonal–cubic phase transitions, hence a suppression of the lattice distortion of $MgMn_2O_4$ is necessary for improving its cathode performance. Feng *et al.* reported thin films of cubic-$MgMn_2O_4$ spinel obtained by PLD methods exhibited higher cathode performances than those for tetragonal-$MgMn_2O_4$ thin films.[17] Although a cubic $MgMn_2O_4$ phase is known as a metastable phase,[26] this phase is only obtained at high-temperature (>950 °C)[27,28] or high-pressure (>15.6 GPa)[29] in bulk.

[a]*Institute of Multidisciplinary Research for Advanced Materials, Tohoku University, 2-1-1 Katahira, Aoba-ku, Sendai, Miyagi, 980-8577, Japan. E-mail: h.kobayashi@tohoku.ac.jp*

[b]*Department of Applied Chemistry, School of Engineering, The University of Tokyo, 7-3-1 Hongo, Bunkyo-ku, Tokyo, 113-8656, Japan*

† Electronic supplementary information (ESI) available. See DOI: 10.1039/c9ra08626a

This journal is © The Royal Society of Chemistry 2019

Open Access Article. Published on 08 November 2019. Downloaded on 4/27/2026 3:35:23 PM.
This article is licensed under a Creative Commons Attribution 3.0 Unported Licence.

Here we demonstrate high cathode performances of ultra-small cubic Mg–Mn spinels synthesized *via* an alcohol reduction process. The process is commonly applied for synthesizing metal nanoparticles as a wet-process, and recently our group applied it for various Mn oxides and showed high catalytic activity for aerobic oxidation reactions.[30–32] We also reported a high-rate capability of $LiMn_2O_4$ nanospinels in a Li-ion battery.[30] In this study, an Mg–Mn spinel oxide (MMO) with approximately 5 nm was prepared by reduction of MnO_4^- in an anhydrous $MgCl_2$ solution in ethanol within 30 min at room temperature, and its cathode performances were investigated.

Results and discussion

Fig. 1a shows synchrotron powder XRD patterns of MMO, $MgMn_2O_4$ spinel prepared by a sol–gel method,[19] and $LiMn_2O_4$ spinel. Peaks of MMO were very broad, indicating the formation of nanocrystals as described later. The XRD pattern of MMO was similar to that of cubic $LiMn_2O_4$ spinel rather than that of tetragonal $MgMn_2O_4$ spinel. In the pseudo radial distribution functions (p-RDF) obtained by a Fourier transform (FT) of k^2-weighted Mn K-edge EXAFS spectra (Fig. 1b), MMO and $LiMn_2O_4$ had a single peak at 2.48 Å attributed to isotropic Mn–Mn pairs, whereas $MgMn_2O_4$ had two peaks at 2.36 Å and 2.76 Å attributed to anisotropic Mn–Mn pairs.[33] The EXAFS spectrum of MMO was well fitted using the first coordination shell consisting of single Mn–O paths (1.891(7) Å) and the second coordination shell consisting of single Mn–Mn paths (2.88(1) Å), suggesting that no Jahn–Teller distortion occurred in MMO to form a cubic phase (Table 1). From the result of ICP elemental analyses of Mg/Mn = 0.40(3) (mol mol^{-1}), the formula of MMO can be described as $Mg_{0.80(6)}Mn_2O_4$ or $(Mg_{0.86(4)}Mn_{0.14(4)})Mn_2O_4$ with the average valence state of $Mn^{3.20(6)+}$ or $Mn^{2.93(7)+}$, respectively. In the former structure, vacancies in cation sites form, while the latter structure is a solid-solution of $MgMn_2O_4$ and Mn_3O_4. Mn K-edge XANES spectra shown in Fig. 1c supported the former structure. The Mn K-edge energy was higher than that of $MgMn_2O_4$ and was similar to that of $LiMn_2O_4$, supporting a higher valence state of Mn in MMO than trivalent. The XRD pattern in Fig. 1a was successfully fitted to $Mg_{0.81(3)}Mn_2O_4$ with the $Fd\bar{3}m$ space group by the Rietveld refinement (Table 2), though the error of refined parameters should become large with such broad XRD patterns. According to the result, and cation-mixing between Mg and Mn is not observed[34] and only vacancy in Mg-site formed.[35] The estimated formula is consistent with the ICP elemental analyses, and estimated bond length of Mn–O and Mn–Mn are 1.988(5) Å and 2.878(1) Å, respectively, supporting the result of EXAFS analysis. The estimated structure is closely similar to the meta-stable cubic-$MgMn_2O_4$ phase[17] or $Mg_yMn_2O_4$ solid solution phase between λ-MnO_2 and $MgMn_2O_4$.[36] Since the reduction reaction of MnO_4^- ion proceeds rapidly to form nanoparticles without heating-up, once a meta-stable phase formed, the phase transition to more stable phase hardly proceed. The cubic phase is obtained probably due to the rapid nucleation of MMO particles at room temperature.

Table 1 Results of EXAFS analysis of MMO[a]

	Coordination number	Distance/Å	Debye–Waller factor/Å^2
First coordination of Mn–O	1.0(2)	1.981(7)	0.003(1)
Second coordination of Mn–Mn	0.7(2)	2.88(1)	0.005(2)

[a] $R = 1.97\%$.

Table 2 Results of the Rietveld refinement

Phase	Space group	Lattice parameters (Å)	Atom	Site	Occupancy (g) and atomic coordination
MMO[a]	$Fd\bar{3}m$	$a = 8.141(4)$	Mg	8b	$g = 0.81(3)$
			Mn	16c	$g = 1.00(1)$
			O	32e	$x = 0.2440(6)$

[a] Partial profile relaxation was applied to 400, 440, and 444 reflection peaks. $R_{wp} = 2.81\%$, $R_p = 2.31\%$, $R_e = 1.65\%$, $S = 1.70$.

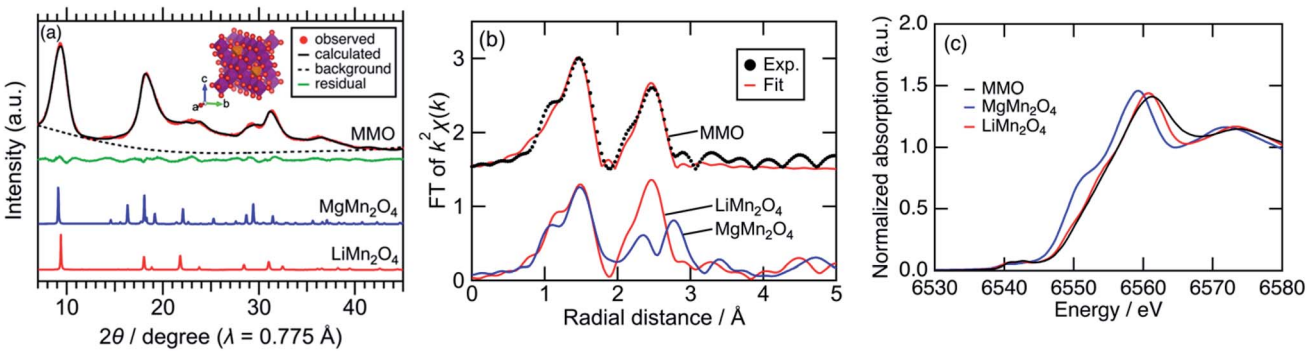

Fig. 1 (a) Synchrotron XRD patterns with the fitting curve by the Rietveld refinement and the schematic illustration for cubic $Mg_{0.81}Mn_2O_4$, (b) p-RDF obtained from the FT of k^2-weighted Mn K-edge EXAFS spectra with the fitting curve by the first and second coordination shell analysis, and (c) Mn K-edge XANES spectra.

Open Access Article. Published on 08 November 2019. Downloaded on 4/27/2026 3:35:23 PM.
This article is licensed under a Creative Commons Attribution 3.0 Unported Licence.

In our previous work, only todorokite-type Mg–Mn binary oxide (OMS-1) was obtained when a hydrous $MgCl_2 \cdot 6H_2O$ dissolved in 2-propanol was used as a Mg-source.[31] In the solution, Mg^{2+} ions were coordinated by water due to their strong Lewis acidic behaviour, and the aqueous complexes were introduced into manganese oxides without dehydration to form OMS-1. In the present work, we found that primary alcohols (*e.g.*, ethanol) have enough solubility of an anhydrous $MgCl_2$ and reducing ability of permanganates instead of secondary alcohols. In the anhydrous condition, Mg^{2+} ions are solvated by ethanol without strong coordination, and are introduced into manganese oxides with desolvation to form a spinel-type Mg–Mn binary oxide. Such difference of products by the amount of water in reaction solutions is also observed in the case of Li–Mn and Co–Mn binary oxides.[31]

Next, surface morphology of MMO particles were investigated. Fig. 2a and b show SEM and TEM images of MMO particles, respectively. These micrographs displayed submicron aggregates of approximately 5 nm nanoparticles with a clear lattice fringe spacing of 0.47 nm, which could be attributed to the 111 plane of the cubic spinel structure. The obtained MMO nanoparticles have much smaller crystallites than previously reported $MgMn_2O_4$ nanoparticles (>10 nm) synthesized by a sol–gel method.[16,18–23] These ultrasmall particles are likely to have been obtained using this wet-process by suppressing the dissolution–recrystallization at ambient temperature and in an anhydrous solvent, while the sol–gel method contains a calcination step at which crystal growth should proceed. A high Brunauer–Emmett–Teller (BET) surface area of 151 $m^2\ g^{-1}$ was also obtained, validating the formation of ultrasmall nanoparticles with below 10 nm in size. However, these large aggregates formed in the drying process should inhibit both electron conduction and Mg^{2+} ion diffusion to degrade electrochemical performances. To suppress such aggregation, graphene was used as an aggregation inhibitor and an electron conducting additive.[30,37] The composite of MMO with graphene (MMO–G) was easily prepared by just adding graphene to the synthetic solution. The Mn K-edge XANES spectrum and the Mg/Mn rate of MMO–G were almost the same as those of MMO, indicating that graphene addition do not affect the structure of MMO (Fig. S1†). The SEM image and corresponding EDX mappings presented in Fig. 2c–f revealed that MMO particles were wrapped by wrinkled graphene to form larger MMO–G secondary particles. Thus, the aggregation of MMO particles could be suppressed by covering the particles with graphene.

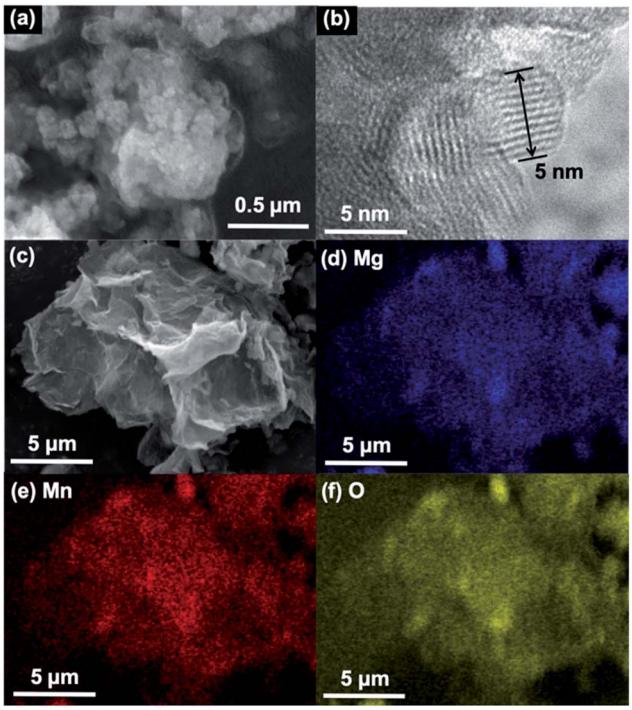

Fig. 2 (a) A SEM and (b) a TEM image of MMO particles. (c) A SEM image and (d–f) EDX mappings of MMO–G composites.

The cathode performances of MMO electrodes with a 0.5 M $Mg(ClO_4)_2/CH_3CN$ electrolyte were investigated using a three-electrode cell at 25 °C with an Ag/Ag^+ reference electrode (+2.6 V *vs.* Mg/Mg^{2+}) and an activated carbon capacitor as a counter electrode (0.0 V *vs.* Ag/Ag^+).[38] Fig. 3a shows the voltage curves of the MMO and MMO–G electrodes at a current density of 10 mA g^{-1}. In the MMO electrode, no plateau was observed during discharge/charge and the discharge capacity was 60 mA h g^{-1}, which was much smaller than that of an ideal one electron reaction per Mn (280 mA h g^{-1}). This small capacity is possibly attributed to the slow diffusion of Mg^{2+} ions into large aggregates of MMO particles. On the other hand, the MMO–G electrode exhibited gentle slopes and a reversible capacity of more than 200 mA h g^{-1}. Since the contribution of the electric double-layer capacitor (EDLC) of the graphene (dotted lines in Fig. 3a) is negligible, the enhancement of the specific capacity derives from the increase in the amount of the redox-active MMO particles. Moreover, dQ/dV curves of the MMO–G electrode exhibited a broad reductive peak at −0.2 V and a sharp oxidative peak at 0.3 V, supporting the redox of MMO (Fig. S2†). The obtained discharge capacity of 230 mA h g^{-1} corresponds to 0.83 electrons transferred per Mn, indicating that the average valence state of Mn changed from +3.19 to +2.36 and the discharge reaction can be expressed by the following equation:

$$Mg_{0.81}Mn_2O_4 + 0.83Mg^{2+} + 1.66e^- \rightarrow Mg_{1.64}Mn_2O_4 \quad (3)$$

Fig. 3b shows Mn K-edge XANES spectra of the MMO–G electrodes. The Mn K-edge was shifted to lower energies during discharge, and almost recovered after re-charge, indicating the reversible redox reaction of Mn. The Mn K-edge position at the full discharge (−1.0 V *vs.* Ag/Ag^+) was approximately in the middle between those of MnO and Mn_2O_3, supporting eqn (3). According to the equation, it is indicated that both eqn (1) and (2) proceeded with a partial formation of rock-salt phase during the discharge.

A rate capability test of the MMO–G electrode was also carried out using the three-electrode cell. Fig. 3c shows voltage curves of an MMO–G electrode at a current density of 190 mA g^{-1}. Even at a moderate current density, reversible discharge/charge proceeded at room temperature with little

Open Access Article. Published on 08 November 2019. Downloaded on 4/27/2026 3:35:23 PM.
This article is licensed under a Creative Commons Attribution 3.0 Unported Licence.

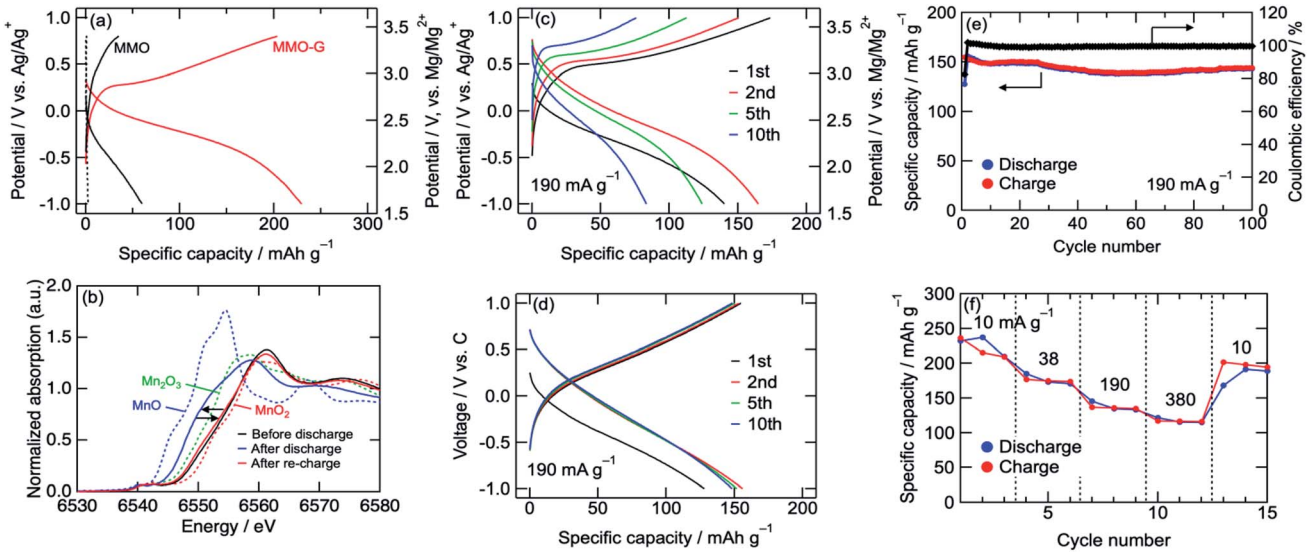

Fig. 3 (a) Voltage curves of MMO and MMO–G cathodes, (b) Mn K-edge XANES spectra of MMO–G cathodes. (c) Voltage curves of MMO–G cathode at 190 mA g^{-1} using a 3-electrode cell or (d) a coin-type cell. (e) Cyclability and (f) rate-capability tests of MMO–G cathode using a coin-type cell.

change in the voltage curves. However, the reversible capacity gradually decreased with the number of cycles, probably due to the dissolution of Mn to the electrolyte or the exfoliation of the electrode from the current collector during discharge/charge.

To reduce the amount of electrolyte and add a confining pressure on the electrode for suppressing the dissolution and exfoliation, a cycle test with a 2032 coin-type cell was investigated. Though the voltage curves with the coin cell slightly reflected the EDLC behaviour of the activated carbon counter electrode, the cell was well cycled more than 100 times without any large capacity loss (Fig. 3d and e). The Mn K-edge position of the electrode after 10th charge was almost the same as that after first charge, suggesting the redox of Mn proceeds at least 10th cycle without decomposition of MMO (Fig. S3†). Furthermore, the cell exhibited a relatively high rate capability (Fig. 3f) even at 380 mA g^{-1} (corresponding to a 1.4 C-rate) compared with previous reports (Table S1†), indicating that the Mg^{2+} intercalation/deintercalation proceeded rapidly due to small diffusion paths in the ultrasmall MMO particles covered by graphene prepared by the alcohol reduction method adopted here.

Conclusions

Cubic spinel-type Mg–Mn oxide nanoparticles with sizes of approximately 5 nm and their composites with graphene as cover were successfully synthesized at room temperature and exhibited a moderate rate cathode performance at room temperature. Both downsizing the primary particles of active materials and suppressing the aggregation of particles are important for further development of cathodes in Mg-ion batteries. Especially in $MgMn_2O_4$ cathode, utilization of metastable cubic phase is important. The alcohol reduction process presented in this letter is a facile method to synthesize ultrasmall cathode materials.

Experimental section

Synthesis of Mg–Mn binary oxides

A precursor n-Bu_4NMnO_4 was synthesized according to a reported procedure.[30] In brief, an aqueous n-Bu_4NBr solution was slowly added to an aqueous $KMnO_4$ solution under vigorous stirring, and the mixed solution was subsequently stirred for 1 h to obtain n-Bu_4NMnO_4. A solution of n-Bu_4NMnO_4 in acetonitrile (2.5 M, 1 mL) was slowly added to an anhydrous $MgCl_2$ solution in ethanol (0.1 M, 100 mL) under vigorous stirring to form a brown colloidal solution. The solution was stirred for 30 min followed by addition of deionized water to form precipitates of the Mg–Mn binary oxide (MMO). The precipitates were collected by membrane filtration, washed with water and ethanol, and dried at 120 °C. A composite of MMO with graphene (MMO–G) was similarly obtained by dispersing 50 mg of graphene nanopowder (G-10, EM Japan Co., Ltd.) in the $MgCl_2$ solution before adding the n-Bu_4NMnO_4 solution. Caution: n-Bu_4NMnO_4 can react violently with itself (the MnO_4^- anion can oxidize the n-Bu_4N^+ cation) and possibly catch fire, hence it should be handled with appropriate care and stored under appropriate conditions (*e.g.* refrigerated conditions).

Material characterization

Synchrotron powder X-ray diffraction (XRD) patterns with a wavelength of $\lambda = 0.775$ Å were collected at the BL5S2 beamline of the Aichi Synchrotron Radiation Center. Samples were charged into Lindeman glass capillaries of 0.5 mm diameter and measured with a rotating stage and a PILATUS 100K detector. The Rietveld refinement was performed using the RIETAN-FP program.[39] Mn K-edge X-ray absorption spectroscopy (XAS) was carried out using the transmission method at the BL11S2 beamline of the Aichi Synchrotron Radiation

Open Access Article. Published on 08 November 2019. Downloaded on 4/27/2026 3:35:23 PM.
This article is licensed under a Creative Commons Attribution 3.0 Unported Licence.

Center. Samples were sealed in an Al-laminated packaging film and attached to a sample holder with Mn foil. Energy calibrations were carried out using the first peak of Mn foil (6539 eV) in a derivative spectrum. Electrode samples were washed with acetonitrile and dried in an Ar-filled glove box before sealing. X-ray absorption near edge structure (XANES) and extended X-ray absorption fine structure (EXAFS) were analyzed by the Athena and Artemis programs.[40] For the EXAFS analysis, the *k*-range of the FT was 3–14 $Å^{-1}$ with a Hanning window of 1 $Å^{-1}$, and the radial distance range of the inverse FT was 1–3 Å. Elemental analyses were performed using inductively coupled plasma atomic emission spectroscopy (ICP-AES) on an Optima 3300XL (PerkinElmer) and a CHN analyzer (Micro Corder JM10, J-Science Lab Co., Ltd.). Scanning electron microscopy (SEM) and Transmission electron microscopy (TEM) images were obtained using JSM-7800F (JEOL) and EM-002B (Topcon), respectively. Brunauer–Emmett–Teller (BET) surface areas were measured by N_2 adsorption at 77 K using BELSORP-mini (MicrotracBEL).

Electrochemical measurements

MMO and MMO–G were mixed with acetylene black (AB; Denka Black, FX-35, Denka Co., Ltd.) and polytetrafluoroethylene (PTFE; Teflon, 6-J, DuPont-Mitsui Fluorochemicals Co., Ltd.) at a weight ratio of 60/30/10 and 80/10/10, respectively. In the MMO–G cathode, MMO/graphene/AB/PTFE = 68/12/10/10 by weight. These mixtures were cut into 8 mm diameter disks of typically 2.5 mg and pressed on an Al mesh current collector to serve as cathodes. For the anodes, a nanoporous activated carbon (Maxsorb®, MSC-30, Kansai Coke and Chemicals Co., Ltd.) was mixed with AB and PTFE at a weight ratio of 8/1/1 and typically 15 mg of the mixture was pressed on a SUS 304 stainless steel mesh current collector. The electrodes were dried at 160 °C under vacuum and introduced into an Ar-filled glove box. For the electrolyte solution, 0.5 M $Mg(ClO_4)_2$ (Sigma-Aldrich) dissolved in acetonitrile (Kanto Chemical Co., Inc.) was prepared and stored over molecular sieves. The cathode, the anode, and the electrolyte were assembled in a three-electrode cell (EC Frontier Co., Ltd.) with an Ag/Ag^+ reference electrode or a 2032 coin-type cell (Hohsen Corp.) with a glass-fiber separator (GA-55, Toyo Roshi Kaisha, Ltd.). The amount of the electrolyte was 2 mL with the three-electrode cell and 0.1 mL with the coin-type cell, respectively. For the reference electrode, a double junction reference electrode was used with internal 0.01 M $AgNO_3$ + 0.1 M n-Bu_4NClO_4 solution in acetonitrile separated by porous glasses. The aforementioned cell preparations were conducted in an Ar-filled glove box. Charge/discharge tests were carried out at 25 °C in constant-current (CC) mode using a multi-channel potentiostat system (VMP3, Bio-Logic Science Instruments) or a battery test system (HJ-1001SD8, Hokuto Denko Corp.). The specific capacity and the current density were calculated on the basis of the weight of MMO in the electrode. Caution: anhydrous perchlorate salts are potentially explosive and should be handled with appropriate care.

Conflicts of interest

There are no conflicts to declare.

Acknowledgements

We thank Prof. Takashi Kyotani and Dr Yasuto Hoshikawa for their supports about measurements of BET surface area. Parts of this work were supported by JSPS Grant-in-Aid for Research Activity Start-up (Grant No. 17H06515) and ALCA-SPRING (Advanced Low Carbon Technology Research and Development Program-Specially Promoted Research for Innovative Next Generation Batteries) from Japan Science and Technology Agency (JST).

Notes and references

1 J.-M. Tarascon and M. Armand, *Nature*, 2001, **414**, 359–367.
2 P. G. Bruce, S. A. Freunberger, L. J. Hardwick and J.-M. Tarascon, *Nat. Mater.*, 2012, **11**, 19–29.
3 R. Black, B. Adams and L. F. Nazar, *Adv. Energy Mater.*, 2012, **2**, 801–815.
4 X. Ji and L. F. Nazar, *J. Mater. Chem.*, 2010, **20**, 9821–9826.
5 J. Muldoon, C. B. Bucur and T. Gregory, *Chem. Rev.*, 2014, **114**, 11683–11720.
6 J. Muldoon, C. B. Bucur and T. Gregory, *Angew. Chem., Int. Ed.*, 2017, **56**, 12064–12084.
7 C. B. Bucur, T. Gregory, A. G. Oliver and J. Muldoon, *J. Phys. Chem. Lett.*, 2015, **6**, 3578–3591.
8 H. D. Yoo, I. Shterenberg, Y. Gofer, G. Gershinsky, N. Pour and D. Aurbach, *Energy Environ. Sci.*, 2013, **6**, 2265–2279.
9 R. Mohtadi and F. Mizuno, *Beilstein J. Nanotechnol.*, 2014, **5**, 1291–1311.
10 E. Levi, M. D. Levi, O. Chasid and D. Aurbach, *J. Electroceram.*, 2009, **22**, 13–19.
11 M. Mao, T. Gao, S. Hou and C. Wang, *Chem. Soc. Rev.*, 2018, **47**, 8804–8841.
12 S. Okamoto, T. Ichitsubo, T. Kawaguchi, Y. Kumagai, F. Oba, S. Yagi, K. Shimokawa, N. Goto, T. Doi and E. Matsubara, *Adv. Sci.*, 2015, **2**, 1500072.
13 H. Kurihara, T. Yajima and S. Suzuki, *Chem. Lett.*, 2008, **37**, 376–377.
14 N. N. Sinha and N. Munichandraiah, *Electrochem. Solid-State Lett.*, 2008, **11**, F23–F26.
15 M. F. Rahman and D. Gerosa, *Optoelectron. Adv. Mater., Rapid Commun.*, 2015, **9**, 1204–1207.
16 M. Cabello, R. Alcántara, F. Nacimiento, G. Ortiz, P. Lavela and J. L. Tirado, *CrystEngComm*, 2015, **17**, 8728–8735.
17 Z. Feng, X. Chen, L. Qiao, A. L. Lipson, T. T. Fister, L. Zeng, C. Kim, T. Yi, N. Sa, D. L. Proffit, A. K. Burrell, J. Cabana, B. J. Ingram, M. D. Biegalski, M. J. Bedzyk and P. Fenter, *ACS Appl. Mater. Interfaces*, 2015, **7**, 28438–28443.
18 J. Yin, A. B. Brady, E. S. Takeuchi, A. C. Marschilok and K. J. Takeuchi, *Chem. Commun.*, 2017, **53**, 3665–3668.
19 Q. D. Truong, M. K. Devaraju, P. D. Tran, Y. Gambe, K. Nayuki, Y. Sasaki and I. Honma, *Chem. Mater.*, 2017, **29**, 6245–6251.

Open Access Article. Published on 08 November 2019. Downloaded on 4/27/2026 3:35:23 PM.
This article is licensed under a Creative Commons Attribution 3.0 Unported Licence.

20 S. Tao, W. Huang, Y. Liu, S. Chen, B. Qian and L. Song, *J. Mater. Chem. A*, 2018, **6**, 8210–8214.
21 G. Liu, Q. Chi, Y. Zhang, Q. Chen, C. Zhang, K. Zhu and D. Cao, *Chem. Commun.*, 2018, **54**, 9474–9477.
22 A. Banu, A. Sakunthala, M. Thamilselvan, P. S. Kumar, K. Suresh and S. Ashwini, *Ceram. Int.*, 2019, **45**, 13072–13085.
23 N. H. Zainol, D. Hambali, Z. Osman, N. Kamarulzaman and R. Rusdi, *Ionics*, 2019, **25**, 133–139.
24 C. Ling, R. Zhang and F. Mizuno, *ACS Appl. Mater. Interfaces*, 2016, **8**, 4508–4515.
25 A. P. B. Sinha, N. R. Sanjana and A. B. Biswas, *Acta Crystallogr.*, 1957, **10**, 439–440.
26 V. P. Barkhatov, V. F. Balakirev, Y. V. Golikov and E. G. Kostitsin, *Phys. Status Solidi A*, 1983, **76**, 57–63.
27 R. Mănăilă and P. Păuşescu, *Phys. Status Solidi B*, 1965, **9**, 385–394.
28 M. Rosenberg and P. Nicolau, *Phys. Status Solidi B*, 1964, **6**, 101–110.
29 L. Malavasi, C. Tealdi, M. Amboage, M. C. Mozzati and G. Flor, *Nucl. Instrum. Methods Phys. Res., Sect. B*, 2005, **238**, 171–174.
30 Y. Miyamoto, Y. Kuroda, T. Uematsu, H. Oshikawa, N. Shibata, Y. Ikuhara, K. Suzuki, M. Hibino, K. Yamaguchi and N. Mizuno, *Sci. Rep.*, 2015, **5**, 15011.
31 Y. Miyamoto, Y. Kuroda, T. Uematsu, H. Oshikawa, N. Shibata, Y. Ikuhara, K. Suzuki, M. Hibino, K. Yamaguchi and N. Mizuno, *ChemNanoMat*, 2016, **2**, 297–306.
32 S. Nakai, T. Uematsu, Y. Ogasawara, K. Suzuki, K. Yamaguchi and N. Mizuno, *ChemCatChem*, 2018, **10**, 1096–1106.
33 H. Yamaguchi, A. Yamada and H. Uwe, *Phys. Rev. B*, 1998, **58**, 8–11.
34 The XRD pattern was fitted using the cation mixing phase $(Mg_{0.8-2x}Mn_{2x})[Mg_xMn_{1-x}]_2O_4$ with $x = 0.006(11)$, indicating the cation mixing of MMO is negligible.
35 The XRD pattern was not fitted successfully with $(Mg_{0.8}Mn_{2x})[Mn_{1-x}]_2O_4$.
36 W. Chen, X. Zhan, B. Luo, Z. Ou, P.-C. Shih, L. Yao, S. Pidaparthy, A. Patra, H. An, P. V. Braun, R. M. Stephens, H. Yang, J.-M. Zuo and Q. Chen, *Nano Lett.*, 2019, **19**, 4712–4720.
37 L. Wang, P. E. Vullum, K. Asheim, X. Wang, A. M. Svensson and F. Vullum-Bruer, *Nano Energy*, 2018, **48**, 227–237.
38 Since acetonitrile-based electrolytes exhibit higher stability at high potential compared with commonly used ether-based electrolytes, the cathode performances were investigated using the acetonitrile-based electrolyte though the electrolyte does not exhibit Mg-deposition/dissolution at the Mg metal anode.
39 F. Izumi and K. Momma, *Solid State Phenom.*, 2007, **130**, 15–20.
40 B. Ravel and M. Newville, *J. Synchrotron Radiat.*, 2005, **12**, 537–541.